INFLUENCE OF SMALL SURFACE DISCONTINUITIES AT THE WELD TOE ON BENDING FATIGUE STRENGTH

V.Gliha*

Results of bending fatigue strength on specimens with synthetic CGHAZ microstructure which were smooth and flawed at the surface were discussed in respect of flaw size and mechanical properties. Specimens were grooved to cause similar stress concentration as that existing at the weld toe. Artificial flaws were single and series of Vickers indentations of the size comparable to the characteristic dimensions of CGHAZ microstructure. Threshold stress intensity factor is a linear function of strength and a parabolic function of flaw size. Bending fatigue strength increases with the strength in the case of significant flaw size and/or harder CGHAZ microstructure. But, it is also increased by local plastic deformation which has happened at the weld toe in the case of insignificant flaw size and/or softer CGHAZ microstructure.

INTRODUCTION

The main fatigue strength controlling parameters of macroscopic homogeneous full penetrated butt weld joints are level of stress concentration and presence of small material discontinuities at the weld toe. Actual fatigue properties of microstructure at the weld toe, where coarse grained heat affected zone (CGHAZ) is usually found, are seldom experimentally studied. Microstructure and properties of CGHAZ depend mainly upon chemical composition of base material (BM), temperature gradient during cooling sequence of weld thermal cycle and of eventual subsequent heat treatment.

The results of bending fatigue strength measurement on different synthetic CGHAZ microstructure are shown and discussed in this article. Stress concentration caused by the transition of weld reinforcement to BM was modelled by a groove. The surface was either smooth or flawed by Vickers indentations.

MATERIAL, SPECIMENS AND EXPERIMENTAL PROCEDURE

The material used was 690 MPa yield stress (CrNiMo) Nionicral 70 (grade HT 80) high strength structural steel. Actual chemical composition and mechanical properties of the steel were: 0.09 C, 0.27 Si, 0.30 Mn, 0.015 P, 0.010 S, 1.05

* Faculty of Mechanical Engineering, Maribor, Slovenia

Cr, 0.27 Mo, 2.63 Ni, 0.07 V, 0.045 Al, 0.026 Ti, 713 MPa yield stress, 764 MPa tensile strength and 170 J impact toughness at -50°C. The steel was made by quenching and tempering. Its microstructure is tempered martensite with some bainite (grain size ~22 μm).

Microstructure of different CGHAZs were made by a computer controlled thermal cycle simulator. The samples were cut off 30 mm thick plate in the rolling direction in size 15x15x70 mm (mechanical properties), 11x11x55 mm (impact toughness) and 15x9x70 mm (fatigue strength). They were heated rapidly (up to 200°/s) to the peak temperature T_p over 1350°C and then cooled down. The consequence of such a weld thermal cycle simulation on as-delivered BM is synthetic microstructure very similar to CGHAZ microstructure of the real weld joint adjacent to the bond. Different cooling times $\Delta t_{8/5}$ were chosen in the range 4-400 s. They correspond to low, standard and high heat input welding.

Dilatation was measured during thermal cycle applications. Temperatures of austenite decomposition start (finish) during cooling and corresponding moments were determined by dilatation curves analysis. Microstructure was metallographic analyzed and hardness was measured. These data were sufficient for CCT diagram designing which is validing under welding conditions (1).

Mechanical properties at room temperature (RT) were tested by hourglass shaped tensile specimens with diameter D_0=4.5 mm and stress concentration factor K_t=1.05 (2). Instantaneous cross section during the test was measured by the circumference change x at the narrowest part of specimen by firm, flexible treat. True stress σ and strain ε at this position are function of load F, D_0 and x. Both were measured and calculated during the test up to the strain of ~0.20.

$$\sigma = K_t \frac{4F}{\pi (D_0 - x/\pi)^2} \; ; \; \varepsilon = -2 \ln \left(1 - \frac{x}{\pi D_0}\right) \quad \ldots\ldots (1)$$

Their relation describes Ludwick's equation.

$$\sigma = A (\varepsilon)^n \quad \ldots\ldots\ldots\ldots\ldots\ldots (2)$$

Strain hardening exponent n and strength coefficient A were estimated by mean slope of log σ-log ε dependence in the range of 0.01-0.20 and by $A=\sigma_{\varepsilon=1}$. True fracture stress σ_f and fracture deformation ε_f were measured by fracture load, final cross-section and undeformed cross-section after each tensile test. Yield stress σ_y and ultimate tensile strength σ_u were determined using engineering σ-ε graphs.

Impact toughness on standard V-notched specimens (10x10x55 mm, 2 mm deep notch) was measured at -40°C.

Bending fatigue strength on grooved specimens (14.5x8x70 mm, 3.2 mm deep rounded groove with r=3 mm) was measured at RT. Grooves were made by machining and subsequent fine polishing, both in the stress direction. Stress concentration factor K_t due to the groove was 1.74 (2). Artificial flaws were single and series of Vickers indentations shown in Figure 1. The flaw dimensions were ~110, ~165, ~220 μm (d) and ~365, ~680 μm (l). Characterizing dimensions of these flaws in the fracture mechanics sense were 35, 50, 70 and 100 μm (3). The specimens were fatigued at ~115 Hz in pulsating bending (R~0). Load range was progressively increasing up to the fatigue crack appearance.

RESULTS

CCT diagram for CGHAZ (thermal cycle to $T_p > 1350°C$) with cooling curves and hardness valid under welding conditions is shown in Figure 2. Ultimate tensile stress σ_u, yield stress σ_y, and nominal bending fatigue strengths σ_{nB}^{0}, σ_{nB}^{35}, σ_{nB}^{70} and σ_{nB}^{100} on cooling time $\Delta t_{8/5}$ at RT are shown in Figure 3. Fracture strength and deformation σ_f, ε_f, strain hardening exponent n at RT and impact toughness vE at -40°C on $\Delta t_{8/5}$ are shown in Figure 4. Data valid for as-delivered BM obtained under the same conditions are also shown in Figure 3 and 4.

DISCUSSION

Solid lines in Figure 2 represent mean values of all measured points, dash lines are logical assumptions based on metallographic analysis. Pure martensitic CGHAZ (M) is formed only at the shortest $\Delta t_{8/5} < 7$ s (first and second cooling curve in Figure 2, $\Delta t_{8/5} \sim 5$ and ~ 6.5 s). As soon as $\Delta t_{8/5}$ attains 7-9 s, some bainite (B) is already present in CGHAZ (third curve, $\Delta t_{8/5} \sim 9$ s). The portion of bainite in CGHAZ increases to $\sim 50\%$ at $\Delta t_{8/5} \sim 25$ s (fourth curve). The result of austenite decomposition at $\Delta t_{8/5} \sim 100$ s is solely bainite (fifth curve). At $\Delta t_{8/5} \sim 400$ s traces of ferrite (F) are found in more or less bainitic CGHAZ (sixth curve). Hardness shown in Figure 2 was measured at the load 100 N (HV10). The hardest is martensitic CGHAZ microstructure (~ 380 HV). As the proportion of bainite grows hardness decreases with $\Delta t_{8/5}$ (7-200 s). Pure bainitic CGHAZ microstructure hardness at $\Delta t_{8/5} = 100$ s is ~ 270 HV. Due to ferrite formation at the start of austenite decomposition during the slowest cooling ($\Delta t_{8/5} = 400$ s) the rest of austenite is enriched on carbon. Bainite which is formed later is harder than that at $\Delta t_{8/5} \sim 100$ s. The reason is higher amount of coagulated cementite in it. This mixture of bainite and a bit of ferrite has hardness ~ 250 HV. Hardness of unaffected BM is ~ 244 HV.

Mechanical properties in Figure 3 decrease with cooling time $\Delta t_{8/5}$ as hardness in Figure 2. Fracture stress σ_f and impact toughness vE attain maximums at ~ 9 s. Maximum fracture deformation ε_f is recorded at higher $\Delta t_{8/5}$ (~ 25 s). Hardening exponent n increases with $\Delta t_{8/5}$, but its two distinct levels are obvious. Lower level is referred to CGHAZ microstructure where martensite prevails (~ 0.07), while higher to that consisting mostly of bainite (~ 0.11). Impact toughness vE of CGHAZ is considerably lower than that of uninfluenced BM at the same temperature. Prior austenite grains of CGHAZ are much coarser (133 μm at $\Delta t_{8/5} \sim 5$ s and 250 μm at 400 s) than grains of BM (22 μm) (1).

The size of artificial small flaw was transformed to equivalent geometrical parameter (EGP) using calculation procedure in reference (3). The supposition was its influence equivalent to that of the crack which shape and size is equal to flaw contour. The suggestion of Murakami and Endo (4) for EGP equal to square root of the area occupied by projecting the flaw onto the plane normal to maximum tensile stress gives almost the same EGP size for single Vickers indentations but not for series of them.

Local stress range at the bottom of grooves $\Delta\sigma$ is higher than nominal bending fatigue strength σ_{nB} due to stress concentration. Ratio $\Delta\sigma/\sigma_y$ versus EGP is shown in Figure 5. Such kind of diagram, suitable to describe short crack influence on fatigue strength, is known by Kitagawa and Takahashi (5). In some

cases $\Delta\sigma$ is greater than yield stress. Figure 6 shows fatigue strength of smooth and flawed specimens in terms of tensile strength. Stress necessary for plastic deformation of infinitesimal volume at the bottom of groove $\sigma_{ny}=\sigma_y/K_t$ is added.

Naturally, maximum tensile stress cannot exceed yield stress not even locally due to plastic deformation. The consequence is R-ratio shift to $R<0$ at the bottom of the groove. CGHAZ microstructure was assumed to be cyclic stable due to its ratio σ_u/σ_y in the range 1.2-1.4 for all treated $\Delta t_{8/5}$ (6). So, local R-ratio was assessed to be $R=(\sigma_y-\Delta\sigma)/\sigma_y$. Fatigue strength at $R=0$ was calculated using well known suggestion of fatigue strength dependence upon mean stress according to Goodman. By means of fatigue strength at $R=0$ and EGP size adequate threshold stress intensity range ΔK_{th} was calculated. The results are linearly strength dependent as already shown in Reference (4). So, ΔK_{th} values were unified according to σ_y and σ_u. Figure 7 represents the dependence of unified ΔK_{th} upon EGP size. Actual ΔK_{th} values from both sides of strength interval valid for single CGHAZ microstructure ($\Delta t_{8/5}\sim$4-5 s) and BM are also given in the figure.

CONCLUSIONS

Small surface discontinuities which size is comparable to the characteristic dimensions of CGHAZ microstructure at the weld toe could influence the fatigue strength of macroscopic homogeneous weld joints. Decreasing of nominal bending fatigue strength with the size of small discontinuities is recorded. As hardest is CGHAZ microstructure at the weld toe as highest is the fatigue strength. On the other hand, possible local plastic deformation at the veld toe in the case softer CGHAZ microstructure referring to longer cooling times causes increasing in nominal bending fatigue strength of weld joints.

Threshold stress intensity of CGHAZ microstructure in the case of small defects is linear function of its strength and parabolic function of defect size.

REFERENCES

(1) Gliha,V. and Taucer,M., Int. J for Joining of Materials, Vol.6, No.3, 1994, pp.116-120.

(2) Peterson,R.E., "Stress Concentration Factors", John Wiley & Sons, New York, 1974.

(3) Murakami,Y., "Stress Intensity Factors Handbook", Pergamon Press, Oxford, 1987.

(4) Murakami,Y., and Endo,M., "Effects of Hardness and Crack Geometries on ΔK_{th} of Small Cracks Emanating from Small Defects", Published articles of Conf. "The Behaviour of Short Fatigue Cracks", Edited by K.J.Miller and E.R.de los Rios, University Press, Cambridge, 1986.

(5) Kitagawa,H., and Takahashi,S., "Applicability of Fracture Mechanics to Very Small Cracks", Proceeding of the Int. Conf. on "Mechanical Behaviour of Materials-ICM 2", Boston, USA, 1976.

(6) Towers,O., J. of Testing and Evaluation, Vol.11, No.1, 1983. pp. 27-33.

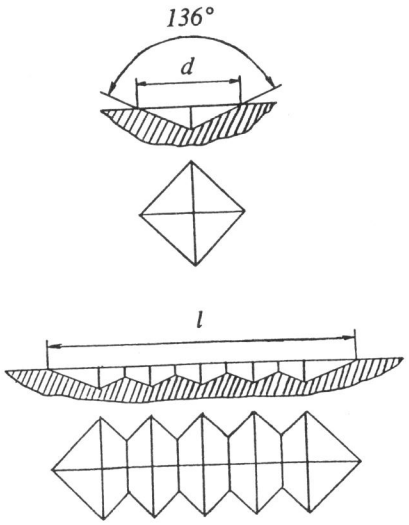

Figure 1 Artificial flaw shapes

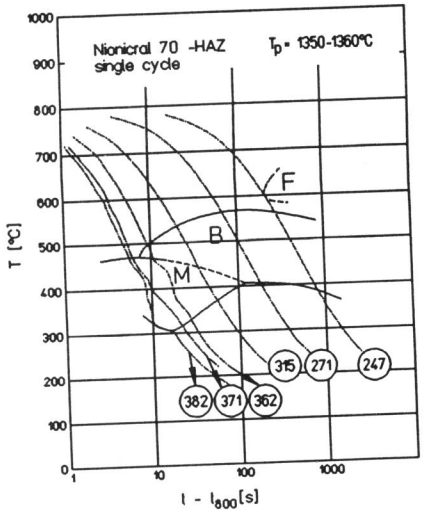

Figure 2 CCT diagram for CGHAZ

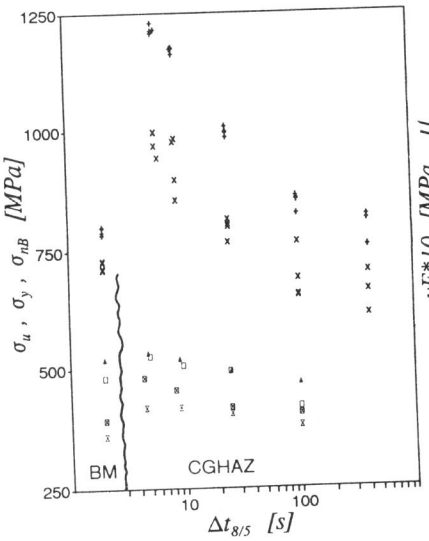

Figure 3 Mechanical properties σ_u, σ_y, σ_{nB}^{0} σ_{nB}^{35} σ_{nB}^{70} σ_{nB}^{100} (+ x ▲ □ ■ ⧖) at RT

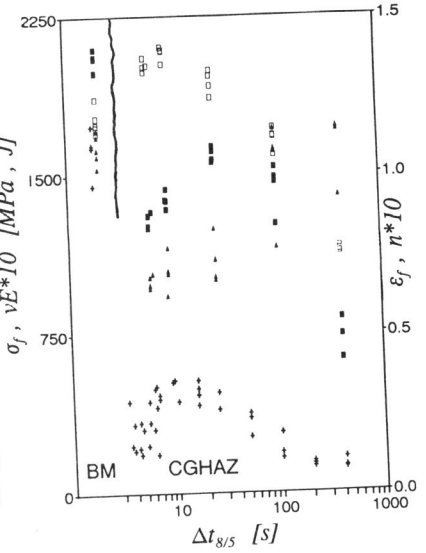

Figure 4 Mechanical properties σ_f, ε_f, n (□ ■ ▲) at RT and vE (+) at -40°C

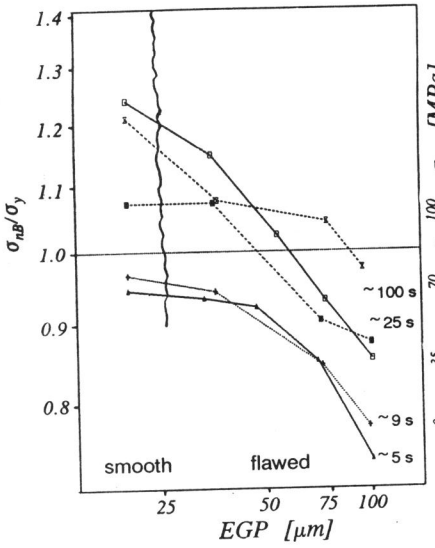

Figure 5 $\Delta\sigma/\sigma_y$ in terms of EGP size for CGHAZ (▲+■x) and BM (○)

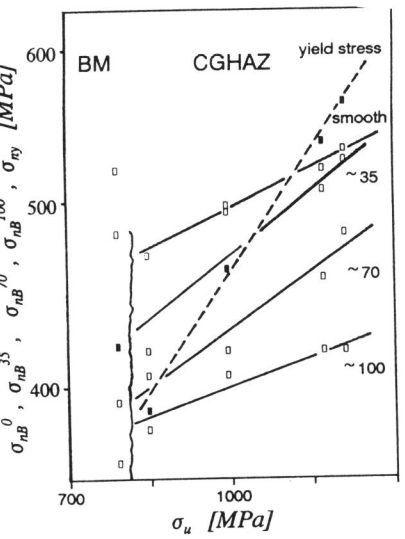

Figure 6 Nominal fatigue strength and yield stress in terms of tensile strength

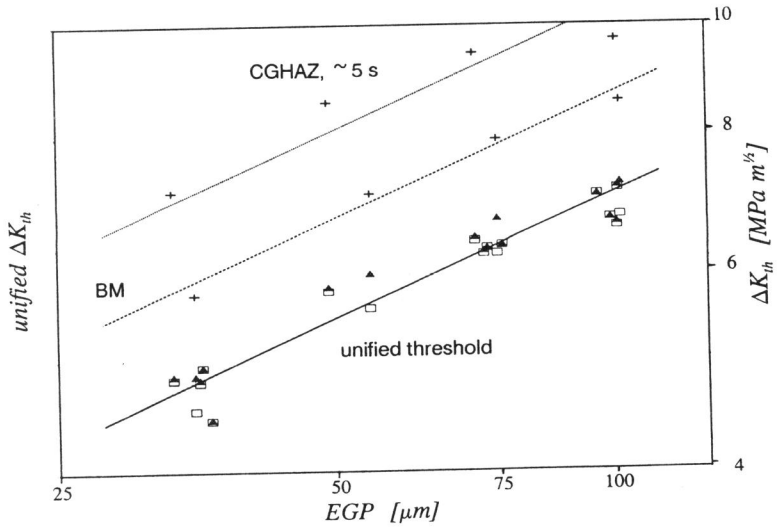

Figure 7 Unified and actual threshold stress intensity factors in terms of EGP size